Available online at www.sciencedirect.com

SCIENCE DIRECT®

Acta Materialia 53 (2005) 3281–3292

Acta MATERIALIA

www.actamat-journals.com

Thermochemical compatibility between alumina and ZrO_2–$GdO_{3/2}$ thermal barrier coatings

R.M. Leckie [a,1], S. Krämer [a], M. Rühle [b], C.G. Levi [a,*]

[a] *Materials Department, University of California, Santa Barbara, CA, USA*
[b] *Max Planck Institut für Metallforschung, Stuttgart, Germany*

Received 4 January 2005; received in revised form 22 March 2005; accepted 27 March 2005
Available online 11 May 2005

Abstract

$Gd_2Zr_2O_7$ and Gd co-doped zirconias are notable examples of materials under consideration for the next generation of thermal barrier coatings, wherein thermochemical and thermomechanical compatibility are critical to the durability of the system. The thermochemical compatibility of $GdO_{1.5}$–ZrO_2 compositions with Al_2O_3 has been investigated using powder compacts and diffusion couples. A tentative isothermal section for the $AlO_{1.5}$–$GdO_{1.5}$–ZrO_2 system at 1200 °C is reported, with additional discussion of the ordering transformation between the fluorite and pyrochlore phases. New light is shed on the long-standing uncertainty on the latter issue. It is shown that addition of $GdO_{1.5}$ to ZrO_2 above ~32% results in the formation of a $GdAlO_3$ interphase, with convoluted morphology and a Gd-depleted fluorite layer above it. The results provide guidelines for the compositional design of emerging thermal barrier materials.

Keywords: Thermal barrier coatings; Gadolinia; Zirconia; Phase equilibria; Thermochemical compatibility

1. Introduction

Thermal barrier systems protect the superalloy components of gas turbine engines increasing their durability and enabling them to operate at temperatures substantially above their nominal capability. The system provides both thermal and chemical protection through a multilayer design. Closest to the surface is an Al-enriched bond-coat (BC) that promotes the formation of a thin (<10 μm) α-Al_2O_3 layer at its outer boundary. This thermally grown oxide (TGO) provides the primary protection against oxidation/corrosion and also acts as a foundation for the actual thermal barrier (TBC) or top-coat. The TBC ($\geqslant$125 μm thick), is typically based on ZrO_2 partially stabilized with 7 ± 1 wt.% Y_2O_3 (7YSZ) deposited by atmospheric plasma spray (APS) or electron-beam physical vapor deposition (EB-PVD). Both processes lead to porous microstructures that benefit the thermal insulation efficiency and allow the coating to tolerate the thermal strains associated with the cyclic temperatures in the engine.

Rare-earth zirconates (REZ) are of interest as alternate thermal barrier materials for advanced gas turbines [1–3]. The drivers are an intrinsically lower thermal conductivity than 7YSZ [2,4–7], and a slower rate of microstructure evolution that helps promote the preservation of the porous architecture for longer times at higher service temperatures [2,3]. A concern, however, is the potential for deleterious interactions between the TBC and the TGO, whose integrity is crucial to the durability of the system [8].

Zirconia and Al_2O_3 are thermochemically compatible, i.e., they do not form interphases and their mutual solubility is very limited [9–11] although large metastable extensions of solubility have been achieved under

---

[*] Corresponding author.
E-mail addresses: rleckie@engineering.ucsb.edu (R.M. Leckie), levic@engineering.ucsb.edu (C.G. Levi).
[1] Tel.: +1 805 680 3561; fax: +1 805 893 8971.

1359-6454/$30.00 © 2005 Acta Materialia Inc. Published by Elsevier Ltd. All rights reserved.
doi:10.1016/j.actamat.2005.03.035

some circumstances [12,13]. In contrast, most of the oxide additives of interest in TBCs (Y, Sc, and RE) exhibit one or more aluminate compounds in their binary equilibria with alumina [14–21]. The implication is that at some critical concentration in TBCs, these additives would tend to form interphases by diffusional interaction with the TGO, degrading the latter and, in consequence, the integrity of the system. For example, Y addition above ~23% $YO_{1.5}$ is expected to induce the formation of garnet at 1250 °C [11,21]. A corollary is the existence of a "safe" concentration, which depends on the type of dopant and, in principle, on the number and concentration of other dopants added. Because these "safer" concentrations are still beneficial in reducing the thermal conductivity, they give rise to a family of co-doped zirconias that compete with the zirconates as potential replacements for 7YSZ in TBCs. In general, these co-doped compositions contain Y plus one or more rare earth cations [22,23] with a total stabilizer content greater than 7% $MO_{1.5}$.

The importance of the thermochemical compatibility between the TGO and novel TBC materials is thus evident, but there is a paucity of information on phase equilibria in $AlO_{1.5}$–$REO_{1.5}$–ZrO_2 systems and the relevant interfacial interactions. The present investigation aims at advancing the understanding of these issues focusing on Gd additions, which are amongst the most promising in terms of their potential for reducing thermal conductivity [4,22,24]. It involves equilibrium studies on samples in which the phase constitution evolved from an initially homogeneous oxide prepared by precursor methods and subsequently subjected to long high temperature treatments. A second activity focuses on the interactions in diffusion couples comprising Gd zirconate TBCs deposited by e-beam on alumina surfaces. The work complements a parallel effort on thermodynamic modeling of the $AlO_{1.5}$–$GdO_{1.5}$–ZrO_2 system [25] and adds to a recent assessment of the $AlO_{1.5}$–$YO_{1.5}$–ZrO_2 system [11]. The ultimate goal is to develop a thermodynamic database for the $AlO_{1.5}$–$GdO_{1.5}$–$YO_{1.5}$–ZrO_2 quaternary as needed to guide the implementation of both co-doped and zirconate materials [8].

The article is organized as follows. The existing information on phase equilibria in the $AlO_{1.5}$–$GdO_{1.5}$–ZrO_2 ternary and the corresponding binaries is briefly reviewed first, followed by a description of the experimental approach. Results of both the equilibrium as well as the diffusional interaction studies are presented next, followed by discussion of the salient points and the relevant conclusions.

2. Background on phase equilibria

Investigation of the phase equilibria in any ternary system starts with the terminal phases and corresponding binary systems. Alumina has only one stable crystalline form, corundum (α, $R\bar{3}c$) whereas both zirconia and gadolinia exhibit polymorphism. ZrO_2 is monoclinic (*m*, $P2_1/c$) at ambient but transforms to tetragonal (*t*, $P4_2/nmc$) at ~1200 °C and then to fluorite (F, $Fm\bar{3}m$) at ~2340 °C. Conversely, Gd_2O_3 evolves through several of the typical rare-earth oxide structures with increasing temperature, from C ($Ia\bar{3}$), to B ($C2/m$) above ~1250 °C, to A ($P\bar{3}m1$) above ~2110 °C, to H_1 ($P6_3/mmc$) above ~2130 °C, and finally to X ($Im\bar{3}m$) above ~2350 °C [26]. There are reasonably complete and consistent phase diagrams published for the $AlO_{1.5}$–$GdO_{1.5}$ [17] and $AlO_{1.5}$–ZrO_2 [10,11,27] systems, but not for $GdO_{1.5}$–ZrO_2. The $AlO_{1.5}$–$GdO_{1.5}$ system exhibits no significant mutual solubility of the terminal oxides and two line compounds, orthorhombic $GdAlO_3$ perovskite (P, *Pbnm*) and monoclinic $Gd_4Al_2O_9$ (M, $P2_1/c1$). There are reports in the literature of a Gd–Al garnet, but that phase appears to be metastable [28]. The $AlO_{1.5}$–ZrO_2 system does not contain compound phases but is reported to show finite solubility, albeit small, of Al^{3+} in ZrO_2 within the tetragonal range [10]. In contrast with Y and trivalent RE additions, wherein addition of dopant beyond the solubility limit of the tetragonal phase yields the cubic structure, excess Al^{3+} in *t*-ZrO_2 leads to melting.

A compilation of phase equilibria information for the $GdO_{1.5}$–ZrO_2 system available in the literature [26,29–33] is presented in Fig. 1, along with schematic phase boundaries suggested by the authors. The calculated diagram by Yokokawa et al. [34] makes some simplifying assumptions and is only qualitatively consistent with the experimental evidence, but serves as a useful guideline.[2] As in other ZrO_2–$REO_{1.5}$ systems, Fig. 1 shows substantial mutual solubility between the oxides, especially in the crystallographically related cubic forms (F and C), as well as one intermediate compound with the pyrochlore structure (Py, $Fd\bar{3}m$). The primary issues for the purposes of the present discussion are the boundaries of the t + F field, which influence the phase stability of co-doped compositions, and the form of the equilibrium between fluorite and pyrochlore. The t + F data is reasonably consistent across three different references [26,32,33]. There is also reasonable agreement on the order–disorder temperature (~1550 °C) for stoichiometric $Gd_2Zr_2O_7$ [29,37], although the order of the transformation is still under debate. The boundaries involving the fluorite, pyrochlore and C–$GdO_{1.5}$ phases,

---

[2] The version of Yokokawa's diagram redrawn in [35] (Fig. Zr-110) suggests a peritectoid reaction between the tetragonal, monoclinic and cubic forms of zirconia, which is inconsistent with the synthesis of non-transformable t' clearly demonstrated for this system [36]. The reason is the incorrect t ↔ m transformation temperature assumed for pure ZrO_2. Examination of other ZrO_2–$REO_{1.5}$ diagrams from Yokokawa redrawn in this collection reveals further inconsistencies in the assumed t ↔ m temperature.

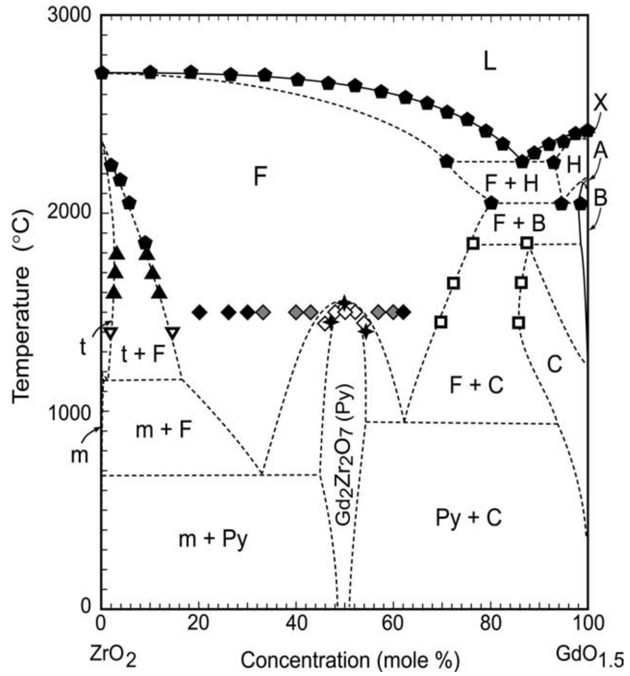

Fig. 1. Suggested $GdO_{1.5}$–ZrO_2 binary phase diagram constructed from a summary of the literature data. Symbols and references: ⬟ [26]; ✦ [29]; □ [30]; ◆ fluorite, ◈ weak pyrochlore peaks, ◇ sharp pyrochlore peaks [31]; ▽ [32]; ▲ [33].

however, are less established, presumably because of the close structural similarity between them and the possibility of partial ordering upon cooling. A homogeneity range of 47–54% $GdO_{1.5}$ was first proposed for the pyrochlore field at ~1400 °C [29] but later studies at 1500 °C revealed the presence of superstructure peaks between 33% and 60% $GdO_{1.5}$ [31], suggesting a broader field. Because such peaks were also observed in compositions annealed at 1600 °C and were rather weak away from the stoichiometric composition, it is possible that they were the result of ordering upon cooling and thus the phase present at high temperature was actually fluorite. Hence, the narrower Py field proposed in [29] is adopted for the initial discussion. A similar problem occurs when determining the boundaries between F and C, wherein ordering involves only the highly mobile anion vacancies. The description in [30] is adopted for this region over the earlier proposal of a wider C field (50–100% $GdO_{1.5}$) with an internal miscibility gap [29].

No significant information on the ternary $AlO_{1.5}$–$GdO_{1.5}$–ZrO_2 was available at the start of this study. However, the similarities between the $YO_{1.5}$ and $GdO_{1.5}$ binaries with ZrO_2 and $AlO_{1.5}$ suggested common features with the $AlO_{1.5}$–$YO_{1.5}$–ZrO_2 system. The latter was then used as an initial "template" with proper modification to account for the absence of a garnet phase in the $AlO_{1.5}$–$GdO_{1.5}$ binary. The present study thus focused on developing a first version of the isothermal section for the $AlO_{1.5}$–$GdO_{1.5}$–ZrO_2 system at 1200 °C, which was taken as an upper bound for the temperature of the TBC/TGO interface in thermal barrier systems.

3. Experimental

Determination of the phase relationships was based on compositions prepared by precursor methods. Equilibration is generally faster in this approach than when using mixtures of powders of the individual oxides because the system starts mixed at the molecular scale and then separates into fine dispersions of the appropriate phases.

Zr acetate solution (Aldrich) and metal nitrate solutions (Alfa Aesar) were used as starting materials. Solutions of the desired stoichiometries were mixed and flash dried onto a hot Teflon™ coated Al substrate ($T >$ 220 °C) to avoid segregation of the components during drying. The dried powders were pyrolyzed at 900 °C in high purity alumina crucibles for 2 h and then pelletized using polyvinyl alcohol solution as a binder. After sintering at 1600 °C for 24 h the pellets were heat treated at 1200 °C for one week, characterized and then heated for an additional two weeks at the same temperature. No significant changes were observed by X-ray diffraction after the one-week treatment, suggesting that equilibration had been achieved.

The phase constitution of the pellets after heat treatment was analyzed using X-ray powder diffractometry (XRD) (Philips X'pert system), scanning electron microscopy (SEM) with energy dispersive X-ray spectroscopy (EDS) (JEOL 6300FEG with Oxford Instruments INCA system, and Philips XL-30 ESEM FEG) and Raman spectroscopy. Electron Probe Microanalysis (EPMA) (Cameca SX50) and TEM/EDS with a $Gd_2Zr_2O_7$ standard were used as appropriate to determine the compositions of the phases. X-ray and electron diffraction with different spatial resolution, as well as Raman, were used to characterize ordering. The Raman analyses for ternary compositions involved (i) subtracting out the perovskite signal when present, (ii) normalizing the intensities of the spectra by the estimated volume fraction of fluorite/pyrochlore in the system, and (iii) adjusting the baseline of the spectra to remove the effect of fluorescence.

The details of interphase formation were studied in diffusion couples between alumina substrates and $Gd_2Zr_2O_7$ coatings (47 μm) produced by electron beam physical vapor deposition (EBPVD) using an in-house research coater. The $Gd_2Zr_2O_7$ sources were 25 mm diameter × 150 mm long pre-alloyed ingots, ~35% porous, (Trans-Tech, Adamstown, MD) and the substrates were either polished sapphire or Fecralloy™ (Goodfellow, Huntingdon, UK) pre-oxidized prior to deposition to yield a polycrystalline TGO. The substrates were heated to a nominal temperature of 1000 °C and rotated at 8 rpm. The "diffusion couples" were heat-treated in air at 1100 or 1200 °C for up to 100 h.

Through-thickness fracture and polished cross-sections of the above specimens were examined in the SEM. In addition, TEM analysis was performed to determine the microstructure and chemistry of interfacial regions on the nanometer scale (JEOL 2010 with Oxford Instruments INCA system). Electron spectroscopic imaging (ESI) was used to determine the spatial distribution of elements using energy filtering TEM (Zeiss EM912, Omega).

4. Results

4.1. Ternary phase equilibria

Fig. 2 depicts the compositions investigated and the tentative 1200 °C isothermal cross-section of the $AlO_{1.5}$–$GdO_{1.5}$–ZrO_2 ternary diagram suggested by the analyses of their phases. Figs. 3–5 summarize XRD, TEM/SAD and Raman spectra on compositions along the $GdO_{1.5}$–ZrO_2 binary. These include both actual binary compositions as well as those defined by subtracting the alumina-bearing phases from the ternary compositions. The approach assumes that there is no significant solubility of Al_2O_3 in the phases present along the $GdO_{1.5}$–ZrO_2 binary, and that the phases along the $AlO_{1.5}$–$GdO_{1.5}$ binary are line compounds [11].

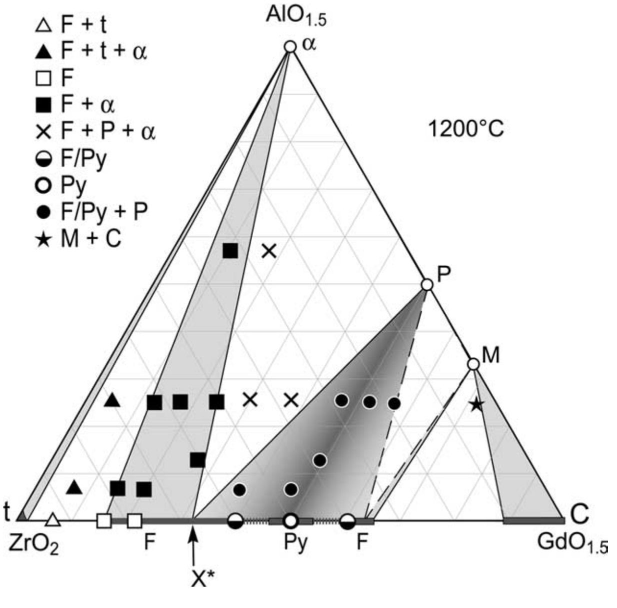

Fig. 2. Tentative isothermal section for $AlO_{1.5}$–$GdO_{1.5}$–ZrO_2 at 1200 °C, showing compositions investigated. The graded shading of the F-P-F triangle denotes the apparently continuous ordering observed within the binary $GdO_{1.5}$–ZrO_2 compositions. Symbols for phases are: t = tetragonal ZrO_2, F = cubic ZrO_2 (fluorite), F/Py = fluorite with varying degrees of pyrochlore-like ordering, Py = pyrochlore, C = cubic rare-earth oxide, M = $Gd_4Al_2O_9$ monoclinic, P = $GdAlO_3$ perovskite, α = alpha alumina (corundum).

Of the ternary compositions the most important are those that help determine the value of the compatibility limit X*, i.e., the three compositions in the α + F + P triangle and those near the boundaries of the α + F and F/Py + P fields (Fig. 2). The X* composition (31.5% $GdO_{1.5}$) was determined by EPMA analysis of the fluorite grains, which are clearly evident in backscattered electron imaging, from the two samples with ~25% $AlO_{1.5}$ within the α + F + P field. TEM/EDS analysis of these fluorite grains found no detectable Al signal. It is noted that garnet was not observed at any point during the heat treatment, in agreement with the latest assessment of the $AlO_{1.5}$–$GdO_{1.5}$ binary [25].

The two compositions in the α + t + F triangle contained m- and t-ZrO_2, as did the binary with 8% $GdO_{1.5}$ along the same tie line. The observed phases are the product of transformation upon cooling and derive from the expected t + F assemblage at 1200 °C. Compositions with Gd:Zr ratios between 0.19 and 0.46 (16–31.5% $GdO_{1.5}$ on the binary) show fluorite alone or in combination with α-Al_2O_3. The absence of monoclinic or tetragonal ZrO_2 was confirmed by Raman spectroscopy, which is particularly sensitive to detect the different polymorphs of ZrO_2. Phase analyses for Gd contents between the P + F(X*) and M + F tie lines of the α + F + P and F + M + C phase triangles, respectively, are complicated by the difficulty in ascertaining whether the Zr–Gd constituent of the microstructure is fluorite, pyrochlore, or a combination of the two. Additional studies of the compositions within this range were thus undertaken in an effort to clarify the form of the fluorite–pyrochlore equilibrium.

4.2. Ordering

XRD analysis of the $(3\,3\,1)_{Py}$ reflection, absent in fluorite, clearly reveals a sharp ordering peak at essentially the stoichiometric composition (49% $GdO_{1.5}$). This peak decays rapidly with departure from stoichiometry and is not detectable at 40% $GdO_{1.5}$ (Fig. 3(a)) or above 53% (not shown). TEM/SAD, however, shows superstructure reflections at compositions between 40% and 61% $GdO_{1.5}$ (Fig. 4). These reflections are diffuse at the extremes of the range and sharpen as the composition approaches the $Gd_2Zr_2O_7$ stoichiometry. Faint diffuse intensity at the same locations is still detectable at compositions as low as 32% $GdO_{1.5}$ (X*) but are definitely absent at 21% and 67% $GdO_{1.5}$. Examining the common $(3\,1\,1)_F/(6\,2\,2)_{Py}$ peak across the lower part of this composition range (Fig. 3(b)) reveals a single peak that shifts gradually to smaller angles with increasing composition. The lattice parameters calculated from these peaks and expressed in relation to the fluorite unit cell are depicted in Fig. 3(c).

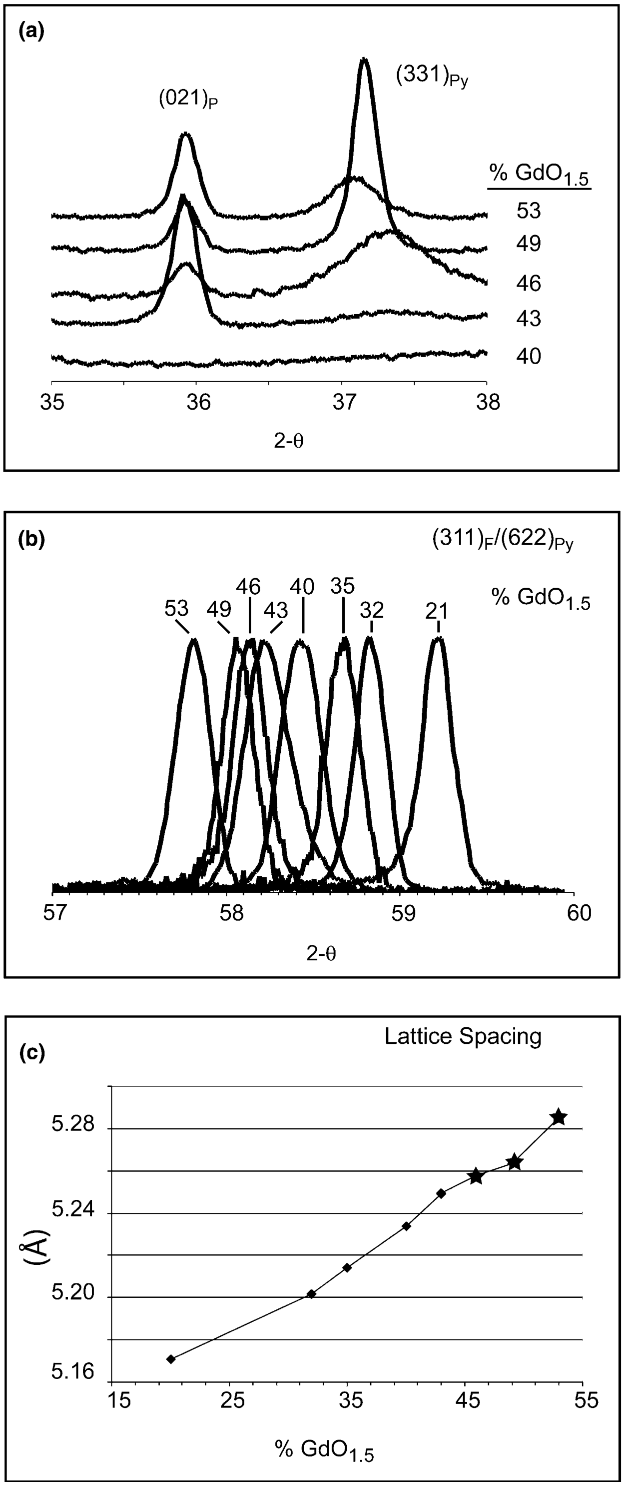

Fig. 3. XRD evidence and derived lattice parameters for the compositions within and around the pyrochlore field. (a) $(3\,3\,1)_{Py}$ superstructure peaks showing increasing and decreasing ordering across the stoichiometric $Gd_2Zr_2O_7$ composition. (b) $(3\,1\,1)_F/(6\,2\,2)_{Py}$ peaks in the same range. (c) Lattice parameter versus Gd content derived from (b) above. Stars mark compositions showing pyrochlore ordering.

The Raman spectra in Fig. 5 exhibit similar trends. The pyrochlore ordering is clearly reflected in the emergence of four peaks between 250 and 650 cm^{-1}. These arise from the O–Gd–O bending, the Gd–O stretch and the two Zr–O bond stretches corresponding to the two types of oxygen positions in the structure [38,39]. Compositions up to 35% $GdO_{1.5}$ show a small and gradual increase in intensity of the broad "peak" between ~250 and ~450 cm^{-1} typical of the fluorite spectrum. This "peak" starts splitting into a doublet (O–Gd–O and Zr–O_{II}) at ~40% $GdO_{1.5}$ and persists up to ~53% $GdO_{1.5}$, while the distinct Gd–O stretch peak is detectable between 43% and 53% $GdO_{1.5}$. The Zr–O_I stretch peak, present already in fluorite, increases and then decreases in intensity as the composition goes through that of the stoichiometric pyrochlore. The 67% $GdO_{1.5}$ spectrum, distinctly different from those of the Gd-lean fluorite and the pyrochlore, is qualitatively consistent with that reported earlier for a similar composition in [38].

4.3. Diffusional interaction

A cross-sectional view of the interface between the sapphire substrate and an as-deposited $Gd_2Zr_2O_7$ coating is shown in Fig. 6(a). The coating was 47 μm thick, with a well-developed (0 0 1) out-of-plane texture and the segmented columnar structure typical of EBPVD TBCs [40]. The coating was adherent at this stage, although it could detach from the substrate during TEM sample preparation, and exhibited no detectable evidence of interaction with the substrate under TEM examination.

Heat treatment at 1200 °C/100 h results in the formation of a distinct interaction zone (~700 nm) at the root of the columns (Fig. 6(b)). A closer view in Fig. 6(b) and the FIB section of Fig. 6(d) reveals this zone to be nominally dense but with an array of pores at its interface with the sapphire substrate. Adherence of the substrate is degraded by the heat treatment, complicating TEM and SEM sample preparation. An oblique SEM view of an area where the coating has detached from the substrate is shown in Fig. 6(c). The fracture appears to have taken place within the porous layer or immediately above it, leaving a reaction product attached to the substrate. The pores are anisotropic in shape with in-plane dimensions a few times their thickness (~150 nm) and cover ~30% of the interfacial area. EDS analysis in the SEM confirms that the sapphire substrate is exposed at the bottom of the pores and the surrounding reaction product contains Gd and Al but not Zr. This interaction zone was also present in the coatings deposited on pre-oxidized Fecralloy™, although in that case the pores appear to be predominantly on the alumina side of the interface, but was not observed in conventional 7YSZ coatings exposed to the same conditions. For $Gd_2Zr_2O_7$ on sapphire, the overall interaction zone was only ~100 nm thick after treatment at 1100 °C for a similar time and was detectable only under TEM. The trend is consistent with the absence of interaction after

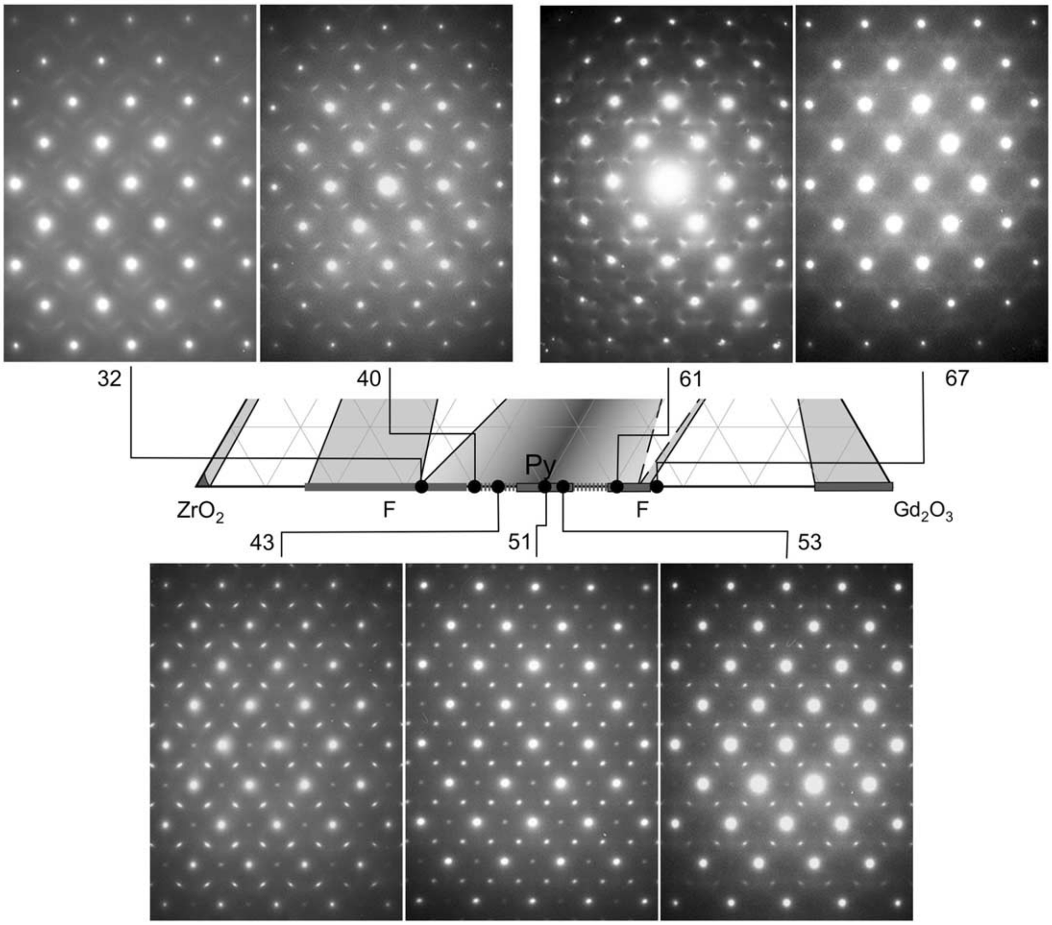

Fig. 4. 110 Zone axis electron diffraction patterns from fluorite-type phases with the indicated Gd-contents. Origin is centered in each picture.

deposition at 1000 °C, where not only the temperature was lower but the exposure was only ~1 h.

TEM images of the reaction layer are shown in Fig. 7. Dark field imaging (Figs. 7(b)–(d)) outlines a two-layer reaction region with a complex morphology. Energy filtering in Figs. 7(e)–(g), coupled with EDS and SAD, confirm that the layer next to the substrate is $GdAlO_3$. The aluminate appears to be continuous and grow epitaxially on the sapphire. Its morphology is complex, comprising a continuous bottom layer intersected by pores and a "scalloped" interface with the sapphire (Fig. 7(a)), and a top region of finger-like protrusions into the original coating material with a length and spacing of several times the thickness of the bottom layer (Fig. 7(c)). Above the $GdAlO_3$there is a Gd-depleted ZrO_2-based layer with the fluorite structure and no significant Al content above the limits of detection. Dark field imaging in Fig. 7(c) reveals this layer is also relatively continuous in plane, except for the places where it is penetrated by the $GdAlO_3$ protrusions, and in the areas examined does not have the same crystallographic orientation as the columns above.

EDS analyses in the TEM reveal the presence of a graded Gd content within the second layer of the interaction zone, as illustrated in Figs. 8(a) and (b). The composition closest to the interface is ~34%Gd but can show significant variability depending on the morphology of the $GdAlO_3$ layer in its vicinity. The material far away from the interface has a higher Gd content than stoichiometric $Gd_2Zr_2O_7$, indicative of preferential deposition of Gd when compared with the measured composition of the source ingot (50%Gd). The profile appears continuous across the interface between the depleted zone and the neighboring column roots.

5. Discussion

The results confirm the assumed similarity of features between the $AlO_{1.5}$–$GdO_{1.5}$–ZrO_2 and $AlO_{1.5}$–$YO_{1.5}$–ZrO_2 systems with some exceptions such as moderately different zirconate compositions, the absence of a garnet phase in the $AlO_{1.5}$–$GdO_{1.5}$ binary and possibly the details of the fluorite–pyrochlore equilibrium. As a first approximation the nature of the ordering phenomena is assumed not to affect significantly the thermochemical compatibility with Al_2O_3 – an assumption to be revisited later – allowing discussion of these two issues separately.

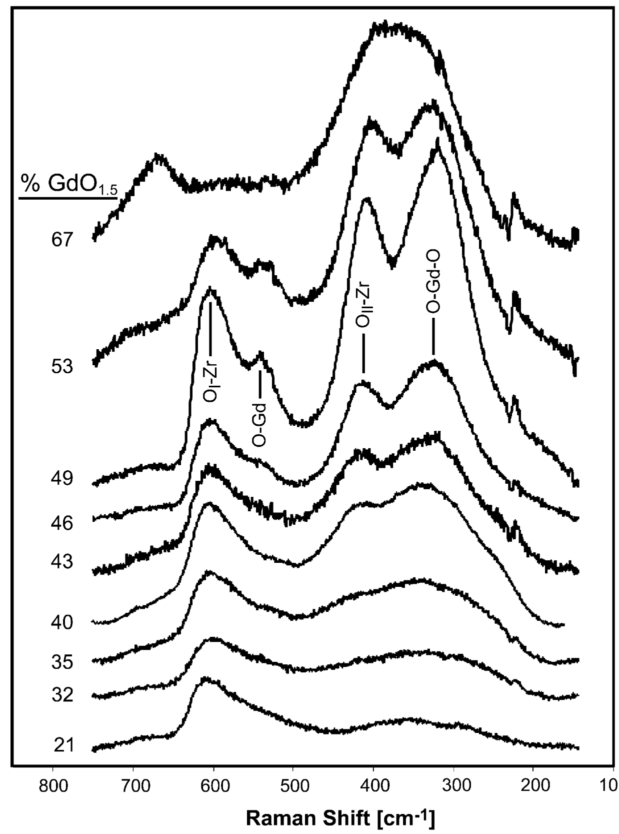

Fig. 5. Raman spectra from samples within and around the pyrochlore-ordering domain. The characteristic pyrochlore peaks are labeled. (The 21% and 40% $GdO_{1.5}$ samples did not contain the perovskite phase and their Raman spectra are presented without the perovskite subtraction or intensity normalization.)

5.1. Compatibility limits

It is now clear that both Y and Gd exhibit compatibility limits with alumina (X*) at compositions within the fluorite field and substantially lower than those of the corresponding zirconates. These two dopants represent the two major types of systems arising when trivalent lanthanide stabilizers are added to ZrO_2, with the larger cations (La → Gd) giving rise to $M_2Zr_2O_7$ pyrochlores and the smaller ones (Y, Er → Lu, Sc)[3] to δ-$M_4Zr_3O_{12}$ type phases. Given the similarities in the phase equilibria of the $LnO_{1.5}$–ZrO_2 systems [34], one may infer from the present results that none of the RE zirconates are likely to be thermodynamically stable in contact with the TGO. The annealed sapphire/$Gd_2Zr_2O_7$ TBC specimens reveal that the kinetics is sufficiently active even at 1100 °C to be a cause for concern over the long term for temperatures more typical of the TGO/TBC interface, viz. 1000–1050 °C. The ensuing degradation of the TGO and the adherence of the TBC indicate implementation of proposed REZs (La, Sm, and Gd) as TBCs may be feasible only by incorporating a suitable diffusion barrier between TBC and TGO. (Arguably, one could design the system to have an interfacial temperature sufficiently low to kinetically suppress the reaction, but the required value would be lower than that in current practice. The approach would thus be inconsistent with the motivation for using REZs to increase the operating capability of the system.) YSZ interlayers have indeed been proposed for zirconate TBCs [3,4,42] but they are justified on the basis of improving adhesion [4] or toughness [42] with no significant discussion of their role as diffusion barriers [8]. Implementation of these barriers is not trivial: the relevant issues will be examined in a forthcoming publication.

The difference in the X* compositions for Y (~23%) and Gd (~32%) is of practical as well as fundamental interest, especially when considering other Ln additions. From a practical perspective, it is an indicator of the relative tolerance of the TGO to different cations in co-doped compositions. When the value of X* is high, as in Gd, it opens the possibility for singly doped compositions that have desirable thermal conductivity and sintering resistance without compromising the TGO. The issue is particularly relevant when comparing with La, in which the value of X* is much smaller (<2% $LaO_{1.5}$) [43] because of the absence of a fluorite field in the binary at the temperatures of interest and the low solubility of La in the tetragonal form [26]. (There is also a degradation of phase stability that limits co-doping of YSZ with the largest RE cations, as discussed elsewhere [44].) The data so far indicates that X* is highest for Gd and decreases for larger (La) and smaller (Y) cations.

The relationship between the dopant and the compatibility limit of the resulting solid solution with alumina is not fully understood. Arguably, X* should be below the composition of the zirconia solid solution in equilibrium with the zirconate in the binary system. Hence, low values for La and possibly for Nd are expected at 1200 °C because large cations have low solubility in the tetragonal phase and upon saturation they form pyrochlore rather than the cubic solid solution. The low solubility can be ascribed to the rapid disruption of the oxygen shift pattern characteristic of the tetragonal phase [45] due to the distortions introduced by the large cation. The preference for pyrochlore over fluorite increases with the size difference between Zr and the dopant, presumably because the pyrochlore ordering can accommodate the distortions better than the random solid solution. The situation is less clear, however, for systems with an equilibrium fluorite field between the tetragonal and pyrochlore phases. With decreasing cation size the homogeneity range of the tetragonal phase increases, and so does the relative

---

[3] Y and Sc are obviously not lanthanides but exhibit common features in their phase equilibria, and $Sc_4Zr_3O_{12}$ is the prototype for the δ-phase [41].

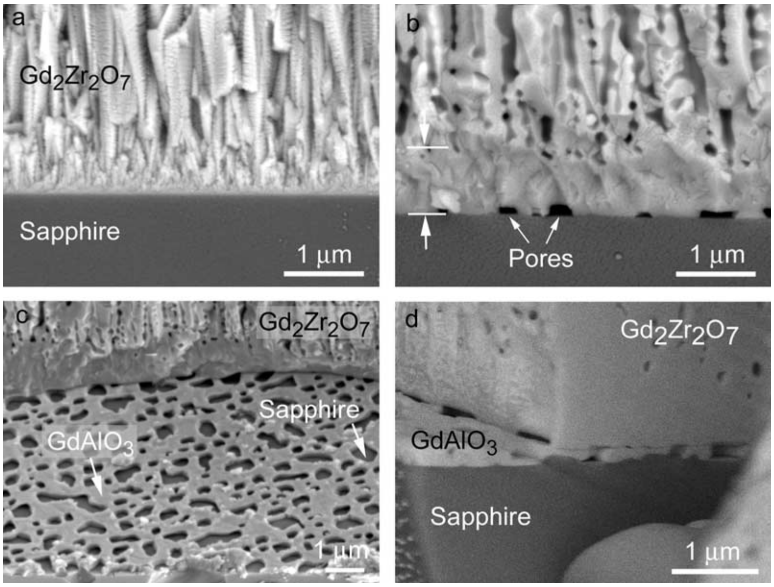

Fig. 6. SEM micrographs of sapphire/$Gd_2Zr_2O_7$ interface. (a) A fracture cross-section of the as deposited interface. (b) A fracture cross-section after 100 h at 1200 °C. Opposing white arrows denote the thickness of the interaction zone. (c) Perspective of the porous reaction layer attached to the sapphire after partial spallation of the coating. The coating and dense region can be seen toward the back of the image. The white areas in the porous region are remnants of coating, the dark grey areas are sapphire visible through the pores, and the light grey areas are $GdAlO_3$. (d) A FIB cut that shows the reaction zone in BEI mode. The underlying pores can be seen above the sapphire.

stability of the fluorite in relation to the pyrochlore. The composition X* is also substantially below the "saturation" limit of the fluorite, although the significance of the latter needs to be discussed in the context of the ordering transformation (below). It is then necessary to examine the possible factors determining the "saturation" limit of fluorite in the presence of alumina, wherein the precipitated phase would be an aluminate rather than the zirconate.

Analysis of the aluminates formed in the $AlO_{1.5}$–$REO_{1.5}$ systems reveals that Gd (and possibly its neighboring elements) behaves substantially differently from the larger and smaller cations. The larger ones form a 1:11 β-alumina phase (e.g., $LaAl_{11}O_{18}$) upon saturation, whereas the smaller ones form garnets (e.g., $Y_3Al_5O_{12}$). Gd, however, is too small to form β-alumina and too large to form garnet, whereupon the first feasible aluminate in the binary becomes the $GdAlO_3$ perovskite (also present in the other systems). The inference is that the concentration of dopant in the fluorite at which the aluminate precipitates depends on the stoichiometry of the aluminate. However, experiments on the $AlO_{1.5}$–$LaO_{1.5}$–ZrO_2 system [43] reveal that the tetragonal phase field can be in equilibrium not only with *β*-alumina but also with the perovskite and the pyrochlore, obviously at different La contents but all within a small range (<2% at 1250 °C [43]). The saturation point to form the aluminate then depends also on the structure and relative stability of the zirconia solid solution, but further research is needed to elucidate this dependence.

5.2. Interphase formation

The diffusion path inferred from the structure and composition profile of the interaction layer in the sapphire/$Gd_2Zr_2O_7$ specimens (Fig. 8(c)) is in agreement with the proposed equilibria (Fig. 2). $GdAlO_3$ forms next to Al_2O_3, with compositions at interface (1) in Fig. 8(a) corresponding to the stoichiometric phases. The composition of the fluorite layer at the interface with $GdAlO_3$ (~34% $GdO_{1.5}$) is slightly above the X* value (~32% $GdO_{1.5}$) in Fig. 2 and the corresponding tie line (2) is within the F + P field. Finally, the composition profile within the fluorite layer and into the original coating columns goes across the prospective fluorite/pyrochlore domain(s) along the $GdO_{1.5}$–ZrO_2 binary (3). The boundary between the Gd-depleted layer and the original columns (Fig. 8(a)) is consistent with the hypothesis of a two-phase F + Py region, but the diffusion profile does not show evidence of the expected discontinuity in Gd concentration across this boundary. Additional analysis with a finer scale probe and on a less convoluted interface is necessary to elucidate this issue. The presence or absence of a F + Py field will be discussed further in the following section.

Analysis of the composition profile in Fig. 8(b) using a 1D model yields an interdiffusion coefficient $\tilde{D} \sim 10^{-16}$ cm^2/s, comparable in magnitude to those characteristic of cation diffusion in bulk ZrO_2 [46,47]. However, the estimated value should be considered preliminary because the diffusion field is not

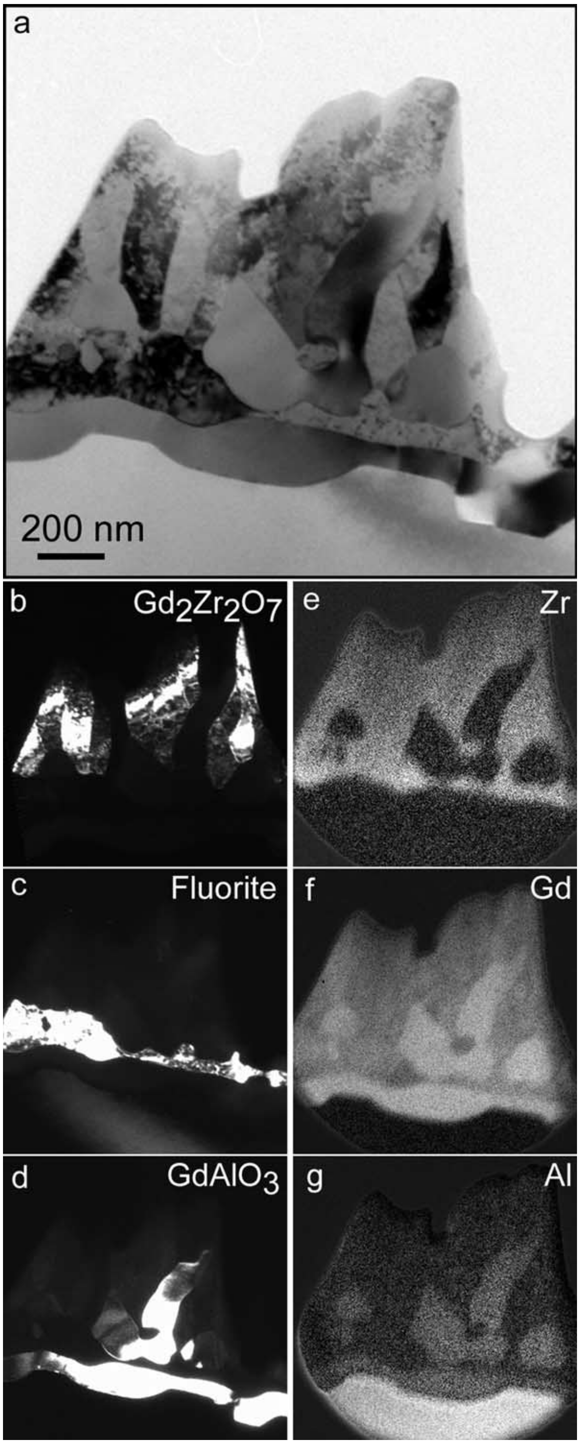

Fig. 7. TEM images that show the structure and chemistry within the reaction zone. (a) Bright field image of the overall structure. (b–d) Dark field images illustrating morphology and orientation of the layers within the reaction zone. (e–f) Energy filtered images revealing the chemistry of the different regions.

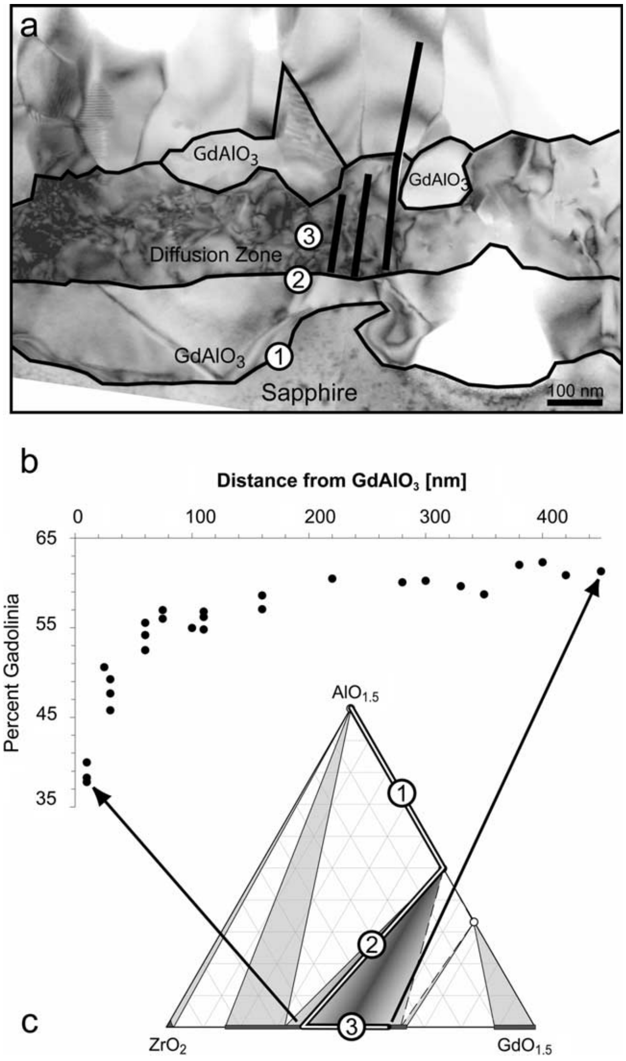

Fig. 8. Microchemical analysis of the interaction zone and corresponding diffusion path. (a) Bright field image of the region analyzed by EDS, marking the scans performed with bold lines. (b) Gd distribution within the fluorite layer, as a function of distance from the $GdAlO_3$ interface. (c) Diffusion path plotted on the proposed isothermal section. The numbers in circles match the areas on the bright field image (a) with the corresponding segments of the diffusion path.

one-dimensional and appears to involve short-circuit paths, as suggested by the $GdAlO_3$ protrusions beyond the Gd-depleted fluorite layer. The protrusions of $GdAlO_3$ and the scalloping of the Al_2O_3/$GdAlO_3$ interface (Fig. 7(a)) suggest counter-diffusion of Al and Gd, respectively. While the protrusions are suggestive of fast diffusion paths, probably along the boundaries between two columns, two issues remain unclear. One is the larger spacing of protrusions compared with that of the column boundaries, and the other is the operating fast diffusion path(s) through the bottom $GdAlO_3$ layer. Al diffusion along the pore surfaces and then up boundaries intersecting them is a likely model, but it remains to be verified.

The mechanism of evolution of the interfacial pores is still under investigation. The height of the pores is comparable to the thickness of the continuous $GdAlO_3$ layer, whereupon the pore-coverage of the interface is also the pore fraction of the aluminate layer, i.e., ~30%. There is a negative volume change (~9%) in the reaction

$$Gd_2Zr_2O_7 + Al_2O_3 \rightarrow 2GdAlO_3 + 2ZrO_2$$

which under constraint could give origin to porosity, but this would account only for ~1/3 of the pore volume. (The actual value is arguably lower since the product is not pure ZrO_2 but rather fluorite heavily doped with Gd.) Coarsening of the pre-existing intercolumnar porosity in the bottom layer of the TBC could also contribute significantly to the observed pore volume. However, it is not immediately obvious why coarsening would favor the pores near the interface and leave a largely dense thick zone above them. Additional porosity could evolve from the asymmetric fluxes of Gd and Al, but this effect remains to be properly quantified.

5.3. The fluorite–pyrochlore equilibrium

The nature of the order–disorder transition in $Gd_2Zr_2O_7$ and the implications to the F + Py equilibrium are the subject of longstanding debate. Some of the literature suggests a continuous ordering transition between fluorite and pyrochlore [37] but the evidence was not considered sufficient to rule out the possibility of a first-order transition with a distinct F + Py field. There is reasonable agreement that the pyrochlores formed by the larger rare earths (Sm, Nd, and La) with ZrO_2 exhibit two-phase equilibria with fluorite and thus a similar behavior would be expected for Gd. The stability of the pyrochlore, however, decreases with RE cation size and is lowest for Gd, with smaller cations forming the δ-$M_4Zr_3O_{12}$ phase instead. The transformation was assumed to be first order in the parallel thermodynamic modeling study [25].

The results from the battery of tests applied in the present study are more consistent with the absence of a two-phase field and by inference a second-order phase transition, although some issues remain unresolved. Raman spectroscopy and electron diffraction both suggest that the degree of ordering decays gradually as the composition departs from the stoichiometric $Gd_2Zr_2O_7$. Diffuse intensity at the superstructure peak locations is observed in the TEM (Fig. 4) even for compositions that do not show detectable ordering in XRD, e.g., 40% $GdO_{1.5}$ (Fig. 3(a)). Raman results for the same composition also show the emergence of the peaks corresponding to the O–Gd–O bend and the Zr–O_{II} stretch (Fig. 5), which are indicative of pyrochlore-like ordering. Conversely, regions with distinctly different compositions or degrees of ordering could not be detected by TEM/EDS analyses in any of the samples examined.

A study of the fluorite–pyrochlore equilibrium in the ZrO_2–$YO_{1.5}$–TiO_2 system, where two-phase separation was not evident in the TEM, clearly demonstrated that that the two phases could be detected by peak splitting of the common reflections in XRD if the lattice parameter difference were significant [48]. The $(3\,1\,1)_F/(6\,2\,2)_{Py}$ peaks in Fig. 3(b) reveals that the technique is sensitive to differences in composition as small as ±3% $GdO_{1.5}$. The absence of splitting or even significant asymmetry in these peaks suggests that all of these samples are essentially single phase after 500 h at 1200 °C. The possible implications are (i) the transformation is second order and there is continuous ordering within the fluorite field, with a maximum at or near the stoichiometric pyrochlore; (ii) a two-phase field, if existing, is probably narrower than 3% in composition; (iii) the system has not yet equilibrated. The lattice parameters derived from the $(3\,1\,1)_F/(6\,2\,2)_{Py}$ peaks (Fig. 3(c)) show some intriguing inflections but no apparent discontinuity between two regions of behavior, consistent with the continuous Gd profile through the "fluorite/pyrochlore boundary" in Fig. 8(a). The presence of the boundary, however, is not immediately consistent with continuous ordering since the original columns were initially in contact with the sapphire and thus the depletion layer would be expected, in principle, to show continuity of the fluorite pattern with varying disorder as it recedes with the growth of $GdAlO_3$.

The hypothesis that the sample may not be fully equilibrated deserves some discussion. The scenario is schematically depicted in the Gibbs energy versus composition diagram of Fig. 9. Whether the sample is produced from precursors or deposited from the vapor, one can readily show that the first phase to crystallize is fluorite. For the powder samples there is also a sintering treatment at 1600 °C, at which point all compositions in the range of interest should be disordered. If the transformation were first order the pyrochlore and fluorite phases could be described by independent free energy curves that would cross at the composition with $T_0(F/Py) = 1200$ °C. All fluorite compositions higher than the crossover point could decrease their free energy by ordering to pyrochlore without necessarily partitioning into two phases, which requires longer-range transport of cations. Because the driving force for phase separation is now substantially reduced, the material could remain in this metastable state for substantial periods of time. The system would then exhibit all signs of continuous ordering as the composition changes across the nominal two-phase field, even though the ultimate equilibrium could indeed involve two phases of different composition. The above scenario could be at the root of the literature debate over this particular equilibrium and will be further explored with longer heat-treatment times.

While the subject of the order–disorder transformation is largely of academic interest, a non-trivial technological implication of the above scenario is that the value of X* in Fig. 2 could change once full equilibrium is attained. The TEM evidence reveals the first signs of

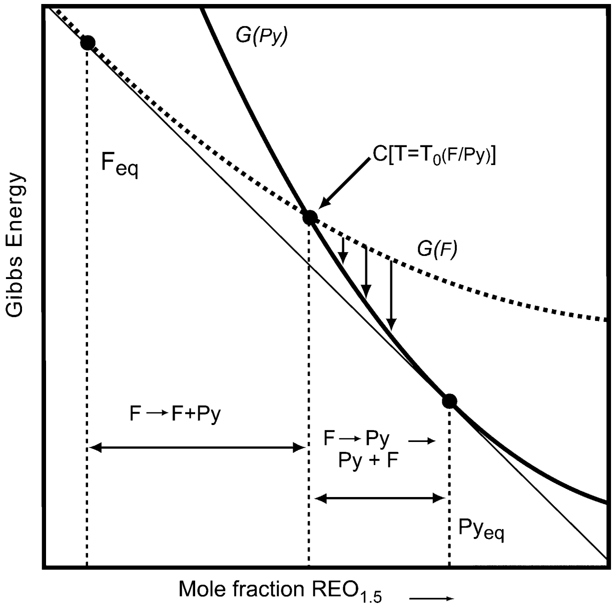

Fig. 9. Schematic free energy curves for a hypothetical two-phase F + Py field. The cross over point corresponds to the composition on the T_0(F/Py) curve. Symbols for phases are: F = fluorite, Py = pyrochlore. The subscript eq denotes the equilibrium compositions.

ordering around X*, which in Fig. 9 would correspond to the crossover point of the free energy curves. Once equilibrium is achieved, the corner of the 3-phase field corresponding to X* could not fall within a two-phase field in the binary. The options are for X* to stay on the fluorite field and thus move to lower compositions, or, less likely, to fall on the pyrochlore field, which would give rise to a Py + α equilibrium and an additional F + Py + α field.

6. Conclusions

The phase equilibria study revealed that the $AlO_{1.5}$–$GdO_{1.5}$–ZrO_2 system exhibits substantial similarity with the $AlO_{1.5}$–$YO_{1.5}$–ZrO_2 system at 1200 °C. The primary differences are the absence of a garnet phase in $AlO_{1.5}$–$GdO_{1.5}$–ZrO_2 and a significant difference in the compatibility limits of the Y- and Gd-doped fluorite solid solutions with α-Al_2O_3. ZrO_2 compositions with >32% $GdO_{1.5}$, when used as thermal barrier coatings, tend to react with the underlying TGO to form a porous $GdAlO_3$ interphase, compromising the integrity of the system and eventually the protective function of the TGO. Excessive $YO_{1.5}$ addition should lead to similar effects in YSZ thermal barriers, but at lower concentrations (>23%) and with formation of garnet.

The growth of the $GdAlO_3$ interphase between $Gd_2Zr_2O_7$ and Al_2O_3 involves both Gd diffusion toward the latter and Al diffusion toward the former, especially through short-circuit paths that may involve the porosity within the $GdAlO_3$. A second layer of Gd-depleted fluorite evolves between the $GdAlO_3$ and the original zirconate. Diffusion through this layer appears to occur at a rate comparable to that of Zr^{4+} bulk diffusion in zirconia. Preliminary evaluation of the interaction kinetics reveals that practical implementation of $Gd_2Zr_2O_7$ (and most likely all rare-earth zirconates) would require interface temperatures substantially below 1100 °C or a suitable diffusion barrier (e.g., 7YSZ) to preclude thermochemical interactions with the TGO. Alternatively, TBCs with Gd contents <32% $GdO_{1.5}$ also offer reduced thermal conductivity and increased sintering resistance without compromising the stability of the system.

Significant insight was gained into the effect of composition on the ordering of pyrochlore and its signatures on the XRD, Raman and TEM/SAD patterns. While most of the evidence is consistent with the idea of continuous ordering, a scenario was advanced in which this continuous transition could be the result of metastable equilibrium within a system that would involve pyrochlore and fluorite phases of different composition under full equilibrium conditions. This scenario, to be further investigated, could explain the ongoing debate in the literature.

Acknowledgements

This investigation was sponsored by a program of international research collaboration between the National Science Foundation (DMR-0099695) and the European Commission (GRD2-200-30211) and made use of the UCSB-MRL Central Facilities supported by NSF under Award No. DMR00-80034. Additional support for S.K. was provided by the Office of Naval Research (MURI/N00014-00-1-0438), and for R.M.L. by an NSF Graduate Fellowship. Helpful discussions with M. Zinkevich, O. Fabrichnaya, C. Wang (Max Planck Institut für Metallforschung, Stuttgart), and Prof. D.R. Clarke (UCSB) are gratefully acknowledged. Interactions with MPI-MF were greatly enhanced by support for C.G.L.'s sabbatical through a Senior Research Award from the Humboldt Foundation.

References

[1] Maloney MJ. US Patent 6,117,560; 2000.
[2] Vassen R, Cao X, Tietz F, Basu D, Stöver D. J Am Ceram Soc 2000;83:2023–8.
[3] Subramanian R. US Patent 6,258,467; 2001.
[4] Maloney MJ. US Patent 6,177,200 B1; 2001.
[5] Wu J, Wei X, Padture NP, Klemens PG, Gell M, Garcia E, et al. J Am Ceram Soc 2002;85:3031–5.
[6] Schelling PK, Phillpot SR, Grimes RW. Philos Mag Lett 2003;84:127–37.
[7] Clarke DR, Levi CG. Ann Rev Mater Res 2003;33:383–417.
[8] Levi CG. Curr Opin Solid State Mater Sci 2004;8:77–91.

[9] Jerebtsov DA, Mikhailov GG, Sverdina SV. Ceram Int 2000;26:821–3.
[10] Lakiza SM, Lopato LM. J Am Ceram Soc 1997;80:893–902.
[11] Fabrichnaya O, Aldinger F. Z Metallkd 2004;95:27–39.
[12] Jayaram V, Levi CG, Whitney T, Mehrabian R. Mater Sci Eng A 1990;A124:65–81.
[13] Balmer ML, Lange FF, Levi CG. J Am Ceram Soc 1994;77:2069–75.
[14] Schneider SJ, Roth RS, Waring JL. J Res Natl Bureau Stand A 1961;65:345–74.
[15] Toropov NA, Kiseleva TP. Russ J Inorg Chem 1961;6:1193–6.
[16] Bondar IA, Vinogradova NV. Bull Acad Sci USSR – Div Chem Sci 1964;5:737–41.
[17] Budnikov PP, Kushakovskii VI, Belavantsev VS. Dokl Chem 1965;165:1177–9.
[18] Rolin M, Thanh PH. Rev Hautes Temp Refract 1965;2:175–85.
[19] Bondar IA, Toropov NA. Bull Acad Sci USSR – Div Chem Sci 1966;2:195–9.
[20] Timofeeva NI, Timofeeva EN, Drozdova LN, Mordovin OA. Inorg Mat (USSR) 1969;5:1476–7.
[21] Lopato LM, Nazarenko LV, Gerasimyuk GI, Shevchenko AV. Neorg Mater 1992;28:835–9.
[22] Nicholls JR, Lawson KJ, Johnstone A, Rickerby DS. Surf Coat Technol 2002;151–152:383–91.
[23] Zhu D, Miller RA. Ceram Eng Sci Proc 2002;23:457–68.
[24] Wu J, Padture NP, Klemens PG, Gell M, Garcia E, Miranzo P, et al. J Mater Res 2002;17:3193–200.
[25] Lakiza SM, Fabrichnaya O, Wang C, Zinkevich M, Aldinger F. J Eur Ceram Soc [in press].
[26] Rouanet A. Rev Int Hautes Temp Refract 1971;8:161–80.
[27] Fisher GR, Manfredo LJ, McNally RN, Doman RC. J Mater Sci 1981;16:3447–51.
[28] Kolitsch U, Seifert HJ, Aldinger F. J Alloys Compd 1997;257:104–14.
[29] Perez y Jorba M. Ann Chim 1962;7:479–511.
[30] Scott HG. J Mater Sci 1978;13:1592–3.
[31] Uehara T, Koto K, Kanamaru F. Solid State Ionics 1987;23:137–43.
[32] Leung DK, Chan CJ, Ruhle M, Lange FF. J Am Ceram Soc 1991;74:2286–92.
[33] Katamura J, Seki T, Sakuma T. J Phase Equilibr 1995;16:315–9.
[34] Yokokawa H, Sakai N, Kawada T, Dokiya M. Phase diagram calculations for ZrO_2 based ceramics: thermodynamic regularities in zirconate formation and solubilities of transition metal oxides. In: Badwal SPS, Bannister MJ, Hannink RHJ, editors. Science and technology of zirconia V. Lancaster (PA): Technomic Publishing; 1990. p. 59–68.
[35] Ondik HM, McMurdie HF, editors. Phase diagrams for zirconium and zirconia systems. Westerville (OH): The American Ceramic Society; 1998.
[36] Rebollo NR, Fabrichnaya O, Levi CG. Z Metallkd 2003;94:163–70.
[37] Haile SM, Meilicke S. The kinetics of ordering in gadolinium zirconate: an unusual oxygen ion conductor. In: Im JS, Park B, Greer AL, Stephenson GB, editors. Thermodynamics and kinetics of phase transformations. Boston (MA): Materials Research Society; 1996. p. 599–604.
[38] Michel D, Perez y Jorba M, Collongues R. J Raman Spectrom 1976;5:163–80.
[39] Oueslati M, Balkanski M, Moon PK, Tuller HL. Raman spectroscopy and structural disorder in $Gd_2(Zr_x,Ti_{1-x})_2O_7$. In: Nazri G, Huggins RA, Shriver DF, editors. Solid state ionics. Pittsburgh (PA): Materials Research Society; 1989. p. 199–206.
[40] Strangman TE. Thin Solid Films 1985;127:93–105.
[41] Scott HG. Acta Crystallogr B 1977;33:281–2.
[42] Dietrich M, Vassen R, Cao X, Stöver D. US Patent Application US 2003/0148148 A1; 2003.
[43] Lakiza SM, Lopato LM. Powder Metall Met Ceram 2000;39:403–6.
[44] Rebollo NR, Gandhi AS, Levi CG. Phase stability issues in emerging TBC systems. In: Opila EJ, Hou P, Maruyama T, Pieraggi B, McNallan M, Shifler D, Wuchina E, editors. Electrochemical society proceedings, PV-2003-16. Pennington (NJ): The Electrochemical Society Inc.; 2003. p. 431–42.
[45] Li P, Chen IW, Penner-Hahn JE. J Am Ceram Soc 1994;77:118–28.
[46] Chien FR, Heuer AH. Philos Mag A 1996;73:681–97.
[47] Kilo M, Taylor MA, Argirusis C, Borchardt G, Lesage B, Weber S, et al. J Appl Phys 2003;94:7547–52.
[48] Schaedler T, Francillon W, Gandhi AS, Grey CP, Sampath S, Levi CG. Acta Mater 2005 [in press].